Understanding the Initial Solidification Behavior for Al-Si Alloy in Cold Chamber High Pressure Die Casting (CC-HPDC) Process Combining Experimental and Modelling Approach

Kun Dou*[1,2], **Yijie Zhang**[2], **Ewan Lordan**[2], **Alain Jacot**[2], **Zhongyun Fan**[2]

1 School of Metallurgy and Environment, Central South University, Changsha, 410083, Hunan, China

2 Brunel Centre for Advanced Solidification Technology (BCAST), Brunel University London, Kingston Lane, Uxbridge, UB8 3PH, United Kingdom

*Corresponding author E-mail: Kun.Dou@csu.edu.cn

Abstract: In the cold chamber high pressure die casting (CC-HPDC) process, alloy solidification in the shot sleeve due to heat loss leads to the formation of externally solidified crystals (ESCs), which have been proven to be closely related to microstructure inhomogeneity and mechanical properties of cast components. In this paper, the solidification behavior of aluminium alloy inside the shot sleeve is studied using a numerical modelling approach. Fluid flow, heat transfer and solidification of aluminium alloy melt inside the shot sleeve are studied using ProCAST software in three dimensions. A comparison between modelling and experiments shows good correspondence. Moreover, the evolution and distribution of ESCs in the shot sleeve along with their dependence on the piston motion profile are analysed accordingly. The results show that after the melt impinges the shot sleeve wall, a thin layer of initial solid forms on the wall with a non-uniform distribution along the sleeve in both the longitudinal and radial directions. With piston movement, the initial solid fraction first increases and then decreases to some extent before being injected into the die cavity. The amount of ESCs at the melt free surface are quantitatively analyzed and validated for different piston motion profiles. The results of this work would be useful in further microstructure and mechanical property variability study of high pressure die casting products.

Key words: Al-Si alloy, HPDC, Solidification, ESCs, microstructure

1. Introduction

The HPDC process has gained considerable interest within the automotive industry, primarily due to its high productivity and excellent cast dimensional accuracy [1-3]. During the cold chamber high pressure die casting process (hereinafter CC-HPDC), the superheated alloy is first poured into a relatively cold shot sleeve (~200 °C) and then injected into the die cavity via the motion of a piston. As the melt impinges the cold wall of the shot sleeve, its temperature decreases below liquidus, forming a thin layer of solid on the sleeve wall. The solid formed at this stage is commonly termed as externally solidified crystals (ESCs). The amount and distribution of ESCs in a cast component varies even under fixed operational conditions, with numerous studies demonstrating their important role in microstructure uniformity and mechanical properties of cast components. Laukli et al. [4-6] studied the solidification microstructure of A356 alloy produced by cold chamber high pressure die casting and concluded that ESCs fraction influences the position of defect band as well as the mechanical properties. Timelli [7] studied the microstructural features of AlSi9Cu3(Fe) alloy produced by CC-HPDC and found that ESCs were concentrated towards the central region of castings and lead to an increase in the average grain size. Fan et al. [8,9] used melt conditioned high pressure die casting technology (MC-HPDC) to refine the ESCs formed inside the shot sleeve, but results shows that microstructure inhomogeneity persisted due to the different cooling conditions in the shot sleeve and die cavity. Such microstructural inhomogeneity could be one potential source of the variability in mechanical properties commonly reported for HPDC components [10,11]. Hence, it is essential to understand how solidification develops inside the shot sleeve and how it will evolve during die filling. In this paper, the formation of ESCs in the shot sleeve during the CC-HPDC process of Al-Si alloy melt (with measured chemical composition 9.66 wt. % Si, 0.64 wt. % Mn, 0.34 wt. % Mg, 0.096 wt. % Fe) is studied using numerical modelling techniques. The influence of piston movement on ESCs evolution is studied quantitatively.

2. Process Modelling

2.1 Model Description

The filling and solidification in the shot sleeve of the CC-HPDC machine is modelled using finite element method (FEM) and can be found in the previous works of the authors [12-14]. The calculation domain which takes into account the entire HPDC machine is shown in **Figure 1**. A detailed view of the shot sleeve region is shown in **Figure 2**. The general FEM mesh size for the entire domain is 1mm, while in the specific thin regions such as ingate and runner, the mesh size of 0.2mm is used. Three dimensional Navier-Stokes equations for mass, momentum and heat transfer are solved using the finite element method. The evolution of the melt free surface during melt flow is modelled using the volume of fluid (VOF) method. Solidification of alloy melt and remelting of the pre-solidified ESCs are described using the enthalpy curve of the alloy calculated with the thermodynamic database provided by ESI. The time duration for the shot sleeve filling is 3s. The melt is poured with an initial temperature of 675°C. The constant pouring amount for the alloy is 750g, which equals to a filling ratio of 20% in the shot sleeve.

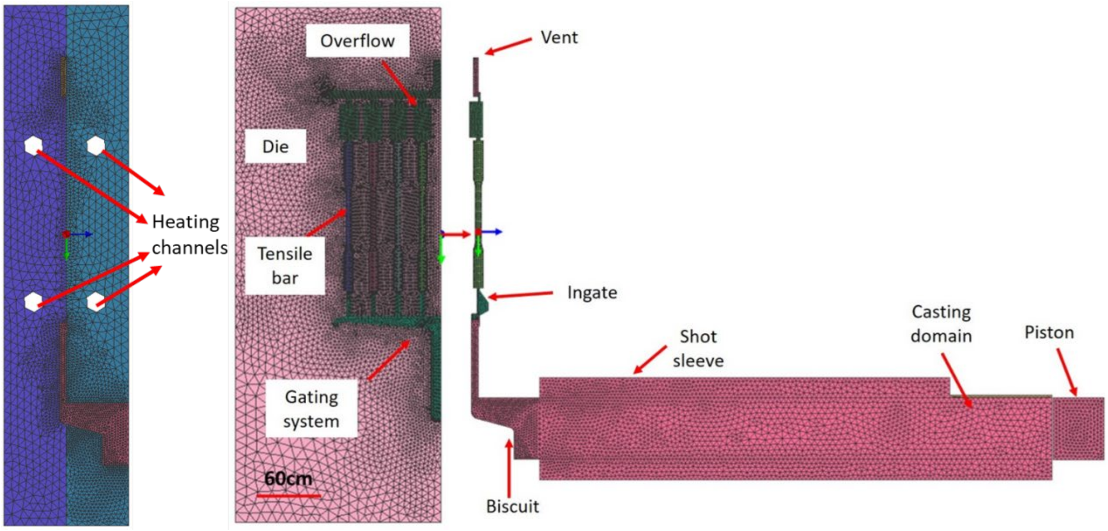

Fig. 1 Geometry and finite element mesh of the modelled HPDC system

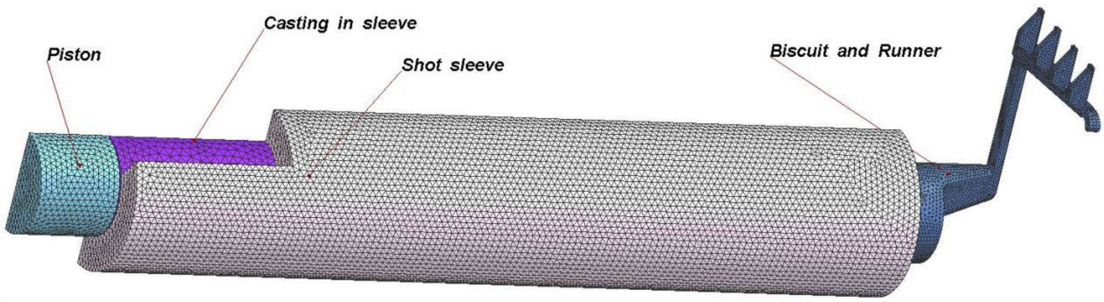

Fig. 2 Geometry and FEM mesh for calculation domain (shot sleeve length: 500mm, inner diameter: 60mm)

2.2 Governing equations

The fluid flow, heat transfer and solidification of the liquid alloy during the HPDC process are calculated mathematically using the following governing equations on the three-dimensional finite element meshes.

Continuity equation:

$$\frac{\partial \rho_l}{\partial t} + \nabla \cdot (\rho_l \langle \boldsymbol{v_l} \rangle) = 0 \qquad \textit{Eq. 1}$$

Momentum equation:

$$\frac{\partial}{\partial t}\left(\frac{\rho_l}{\boldsymbol{g}} \langle \boldsymbol{v_l} \rangle\right) + \nabla \cdot \left(\frac{\rho_l}{\boldsymbol{g}^2} \langle \boldsymbol{v_l} \rangle \langle \boldsymbol{v_l} \rangle\right) + \nabla p - \nabla \cdot \left(\frac{\mu_l^{eff}}{\boldsymbol{g}} [\nabla \langle \boldsymbol{v_l} \rangle + \nabla \langle \boldsymbol{v_l} \rangle^T]\right)$$

$$= \rho \boldsymbol{g} - \mu_l K^{-1} \langle \boldsymbol{v_l} \rangle \qquad \textit{Eq. 2}$$

Energy equations:

$$\frac{\partial (\rho h)}{\partial t} + \nabla \cdot (\rho \boldsymbol{g}\, h\, \langle \boldsymbol{v_l} \rangle) = \nabla \cdot (\kappa \nabla T) + S \qquad \textit{Eq. 3}$$

$$h(T) = \int_0^T C_P(T)dT + L(1 - f_S(T)) \qquad \textit{Eq. 4}$$

In the above equations, $\langle \boldsymbol{v} \rangle_l$ is the intrinsic phase averaged velocity, ρ is the density, p is the pressure, μ_l is the melt viscosity, T is the temperature, C_p is the specific heat, L is the latent heat of solidification, and h is the enthalpy.

2.3 Parameter Adjustment

According to relevant research from Helenius, Raimo, et al [15] and Shoumei Xiong et al. [16-18]. The shot sleeve wall condition would differ along sleeve length direction due to oxides formation, non-uniform lubricant distribution as well as surface roughness, as is depicted in **Figure 3**.

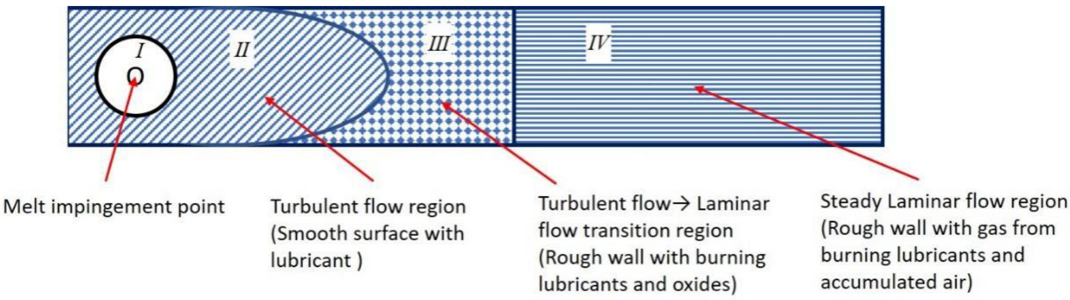

Fig. 3 Mechanism for melt flow development in shot sleeve, adapted from reference [15]

Figure 3 illustrates that the sleeve wall may be divided into four characteristic regions. As the melt impinges the sleeve wall (zone I), the flow is initially turbulent for some distance along the longitudinal axis of the shot sleeve (zone II, covered by lubricant). Then, in zone III with reduced lubrication, the flow regime transforms from turbulent to laminar due to the steady melt velocity and friction induced by the rough sleeve wall. In the meantime, gas will form due to the burning of lubricant and residual air at the sleeve wall may be entrained into the melt. As the melt enters zone IV, flow ceases due to the decrease in melt temperature and gas pores accumulate at melt-sleeve wall interface, which will influence further solidification of the melt.

Whilst all these phenomena would influence the heat transfer and flow of aluminium melt, the model needs to be properly modified before it can be used for further analysis. In ProCAST software, two parameters WALLF and WSHEAR are responsible for adjusting the fluid flow behavior near to the wall. Whilst the heat transfer calculations can be properly adjusted by modifying the interfacial heat transfer coefficient (iHTC) between the melt and sleeve wall. In this paper, six combinations of time-dependent WALLF, WSHEAR and iHTC values are compared before a suitable selection is obtained and applied in the model. The description of these parameters could be referenced from the previous work of the authors [12]. The applied value of WSHEAR is 2, and the time-denepdent iHTCs and WALLF values are shown in Figure 4(a) and (b).

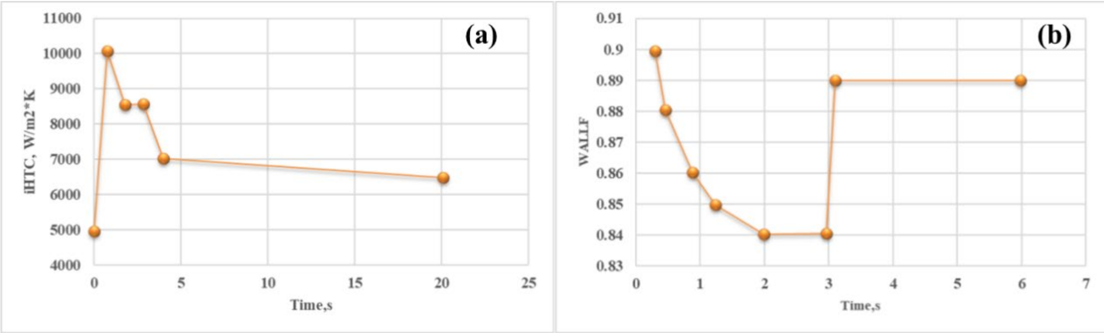

Fig. 4 Time-dependent (a) iHTC and (b) WALLF values used in this work

2.4 Model Validation

Based on these, a filling test was conducted in the shot sleeve with the exact same condition as the modelling the shapes of the solid formed in the sleeve were compared with actual filling tests and the temperature distributions at different locations in the shot sleeve were obtained using thermal couples which positions were shown in **Figure 5**. The calculated and measured temperatures curves are shown in **Figure 6**, main discrepancies were observed when the melt came into initial contact with the thermocouples, which attribute to their relatively high response time (~1 s). In addition, the shapes of the metal after partial solidification in the sleeve closely resemble those predicted, as is indicated in **Figure 7**.

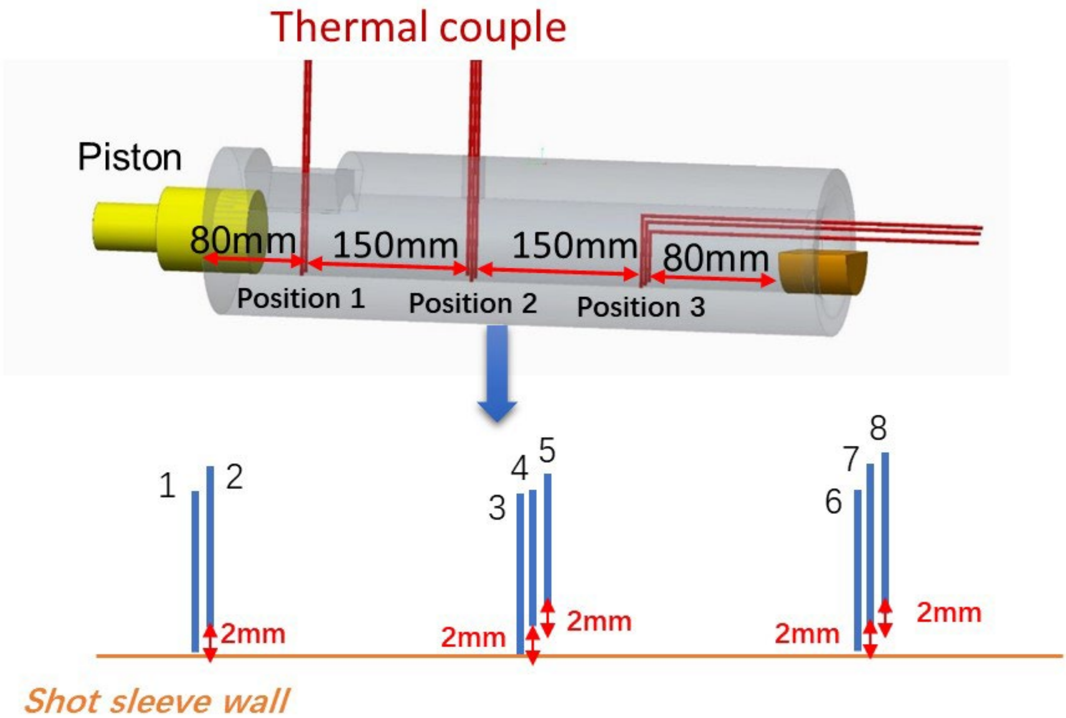

Fig. 5 Configuration of temperature measurements during shot sleeve filling experiments

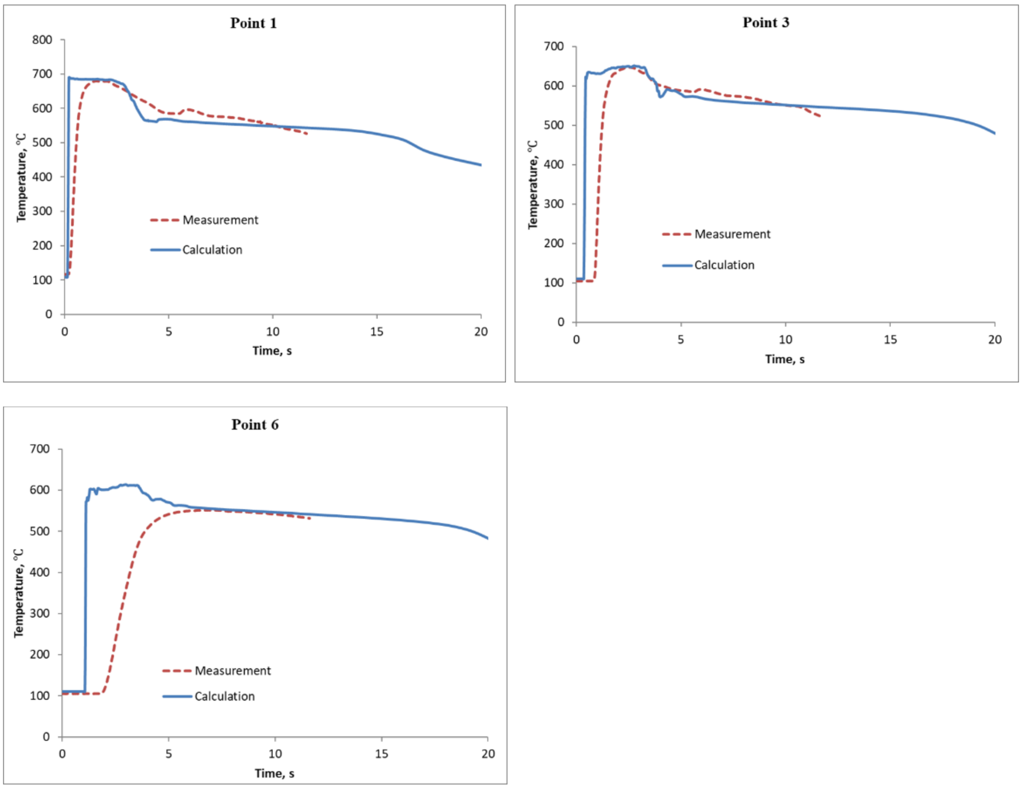

Fig. 6 Comparison of measured and calculated temperature curves at Point 1, Point 3 and Point 6, as is indicated in Fig. 4

Fig. 7 Comparison of solid shape in sleeve between filling tests and model calculations

3. Modelling Results

3.1 Initial solidification of melt before piston movement

Figure 8 shows the evolution of the melt free surface (the interface between melt and the air in shot sleeve and die cavity) and turbulence in the shot sleeve. It could be observed that turbulence occurs the moment the melt collides the sleeve wall and it calms as the continual filling the sleeve. **Figure 9** reveals the solidification of the melt in the sleeve when filling for 5s. Combining above two figures, it could be observed that melt solidifies as soon as it contacts the sleeve wall. At the initial filling stage, with down-pouring of liquid metal from the above pouring hole, the melt flow is turbulent at the contact point, then two flows develop. The left flow would first flow towards the piston and be forced back. Due to cooling water circulation inside the piston, more solid forms near to the piston region. The right flow develops towards the far end of sleeve and fluid velocity decreases, attributed to two phenomena: (1) continual heat loss of melt along the longitudinal axis of the sleeve, which causes increase of melt viscosity and (2) friction between the sleeve and melt.

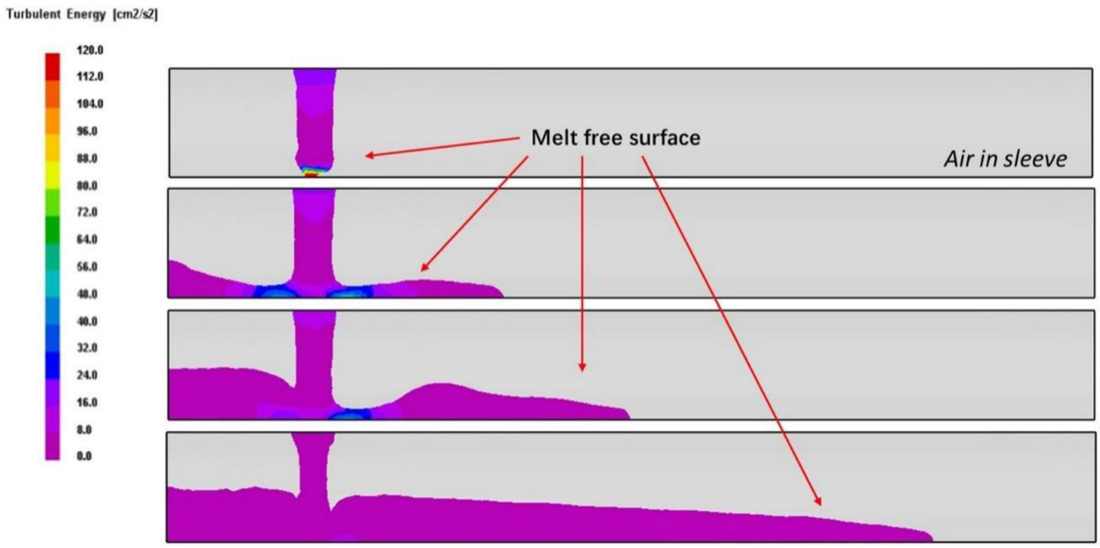

Fig. 8 Evolution of melt free surface and turbulence in the shot sleeve, with colour map indicating turbulent energy at different locations-2D section cut from longitudinal axis of sleeve

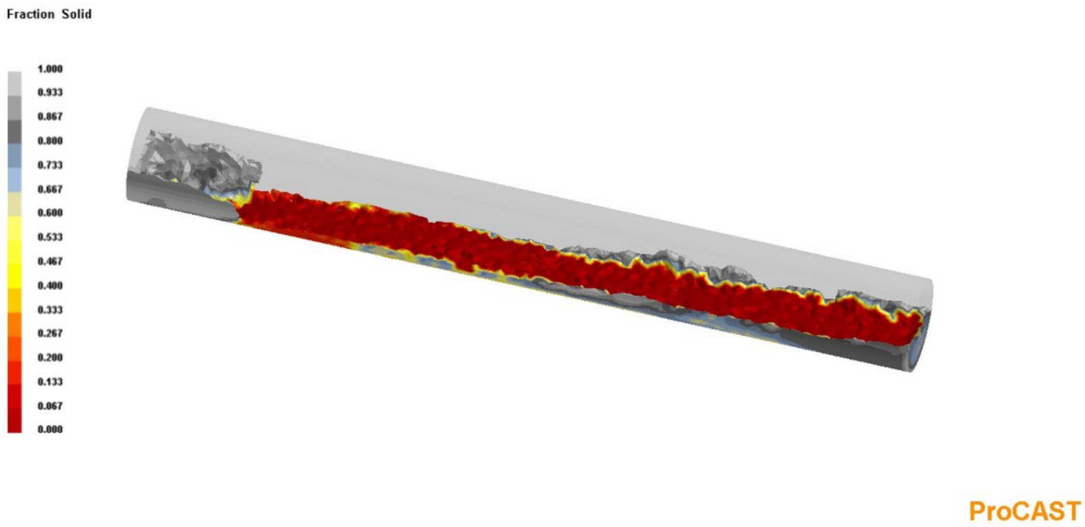

Fig. 9 Solidification of the melt in shot sleeve after filling for 5s (color bar shows the solid fraction, with piston side on the left)

Figure 10 reveals the solid-melt distribution on several sleeve radical direction slices. As illustrated in **Figure 10,** ESCs tend to distribute non-uniformly along the shot sleeve, with more ESCs found towards the piston and biscuit regions, whilst less ESCs are observed in the middle. The ESCs distribution can be further examined by taking a longitudinal slice as in **Figure 11**, it could be noticed that in a steady filling process, the minimum solid thickness location is below the pouring hole. Based on **Figure 11**, the solid fraction curve along line

AB (3mm above sleeve bottom) is plotted as in **Figure 12**. It could be noticed that after filling for 5s, the solid fraction at piston end is ~1% while at the other side of sleeve, solid fraction is ~0.5%. The solid fraction drops below 0.1 gradually from both ends of sleeve to centre due to slow heat transfer and steady flow of melt.

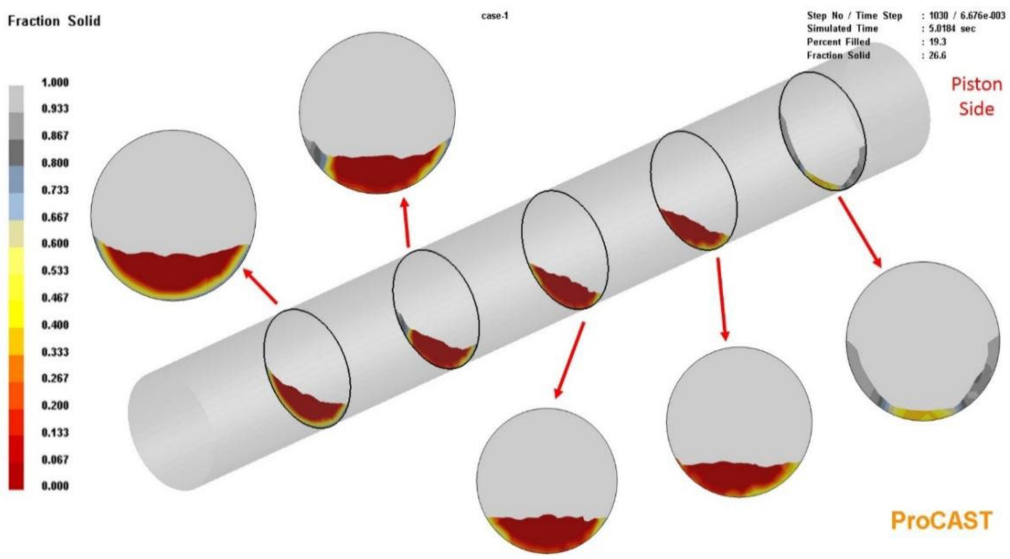

Fig. 10 Slice view for solid fraction along sleeve length direction

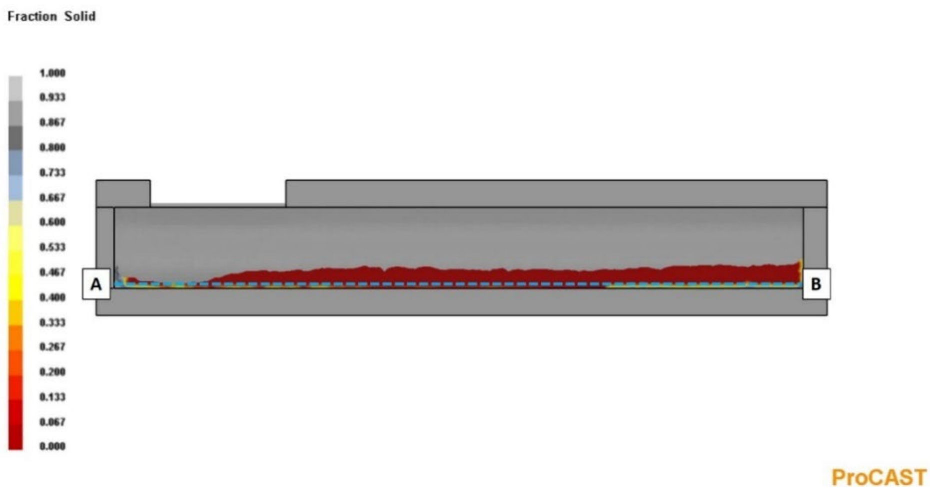

Fig. 11 Solid fraction longitude cross-section of sleeve after filling for 5s

(Piston at side A)

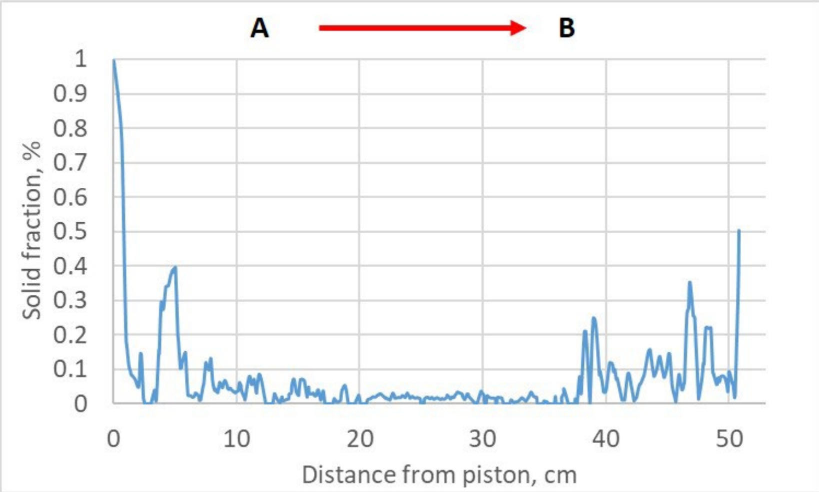

Fig. 12 Solid fraction along AB line in Fig. 10 after filling for 5s

3.2 Evolution of melt solidification during piston movement

During the actual CC-HPDC processing, piston velocity will clearly influence the evolution of ESCs in the shot sleeve and the following injection as well as their distribution inside the die cavity. Here in this paper, the evolution of ESCs in the shot sleeve with three different piston velocity profiles are analyzed numerically. The piston movement profiles used in this work are illustrated in **Figure 13**. The first stage velocity varies among 0-0.2-0.3m/s, 0-0.4-0.6m/s and 0-0.6-1m/s in Profile-1, Profile-2 and Profile-3, respectively. The second stage velocity of 3.6m/s is kept constant in all the three piston velocity profiles.

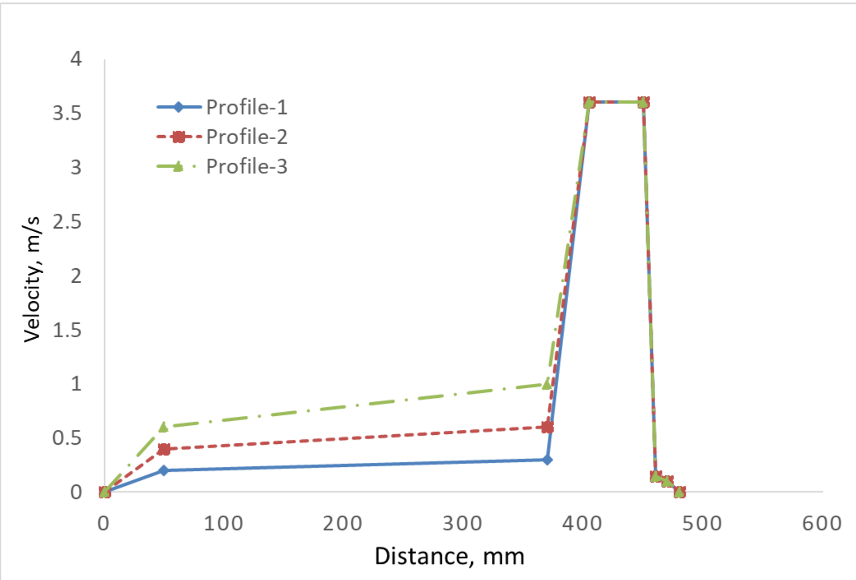

Fig. 13 Piston movement profiles used in this work

Figure 14 depicts the evolution of ESCs during piston movement in shot sleeve from side view (left) and top view (right) with Profile-1. It could be seen that during the first stage piston movement where piston moves forward at low velocity, ESCs accumulate towards the piston and mix with the melt until the remaining sleeve chamber is filled with the mixture. Afterwards, the piston velocity increases to secondary stage velocity of 3.6m/s for injection into the die cavity. The solid distribution from sleeve top to bottom is non-uniform according to the colour map shown here. To further investigate this, three slices are taken inside the chamber before fast shot stage starts in shot sleeve, as shown in **Figure 15**. It is worth noting that the solid fraction (fs) at melt and sleeve wall interface is larger compared with melt in sleeve central region, which is a result of strong cooling condition at sleeve wall. Moreover, fs plots along line A1-A, B1-B and C1-C are obtained as in **Figure 16**. In sleeve radical direction, the maximum solid fraction appears at sleeve bottom with a range between 0.7%-1%. Solid fraction of the mixture approximates zero in sleeve central region while continually increases to the range of 0.02%~0.07% at sleeve top. Comparing the solid fraction distribution along the longitudinal length of the shot sleeve, the fs curve along C1-C exhibits largest values compared with the other two, which means that more ESCs tend to aggregate near to the piston region compared to any other region.

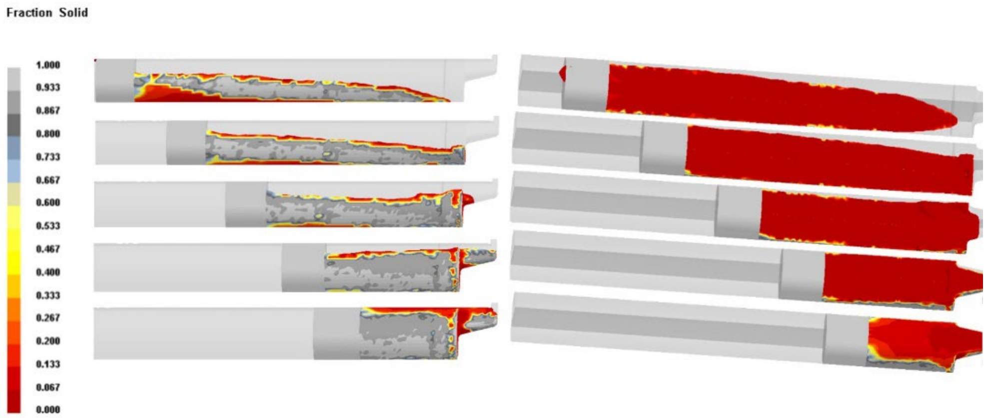

Fig. 14 Solid fraction during piston movement in shot sleeve from side view (left) and top view (right) with Profile-1 in Fig. 12

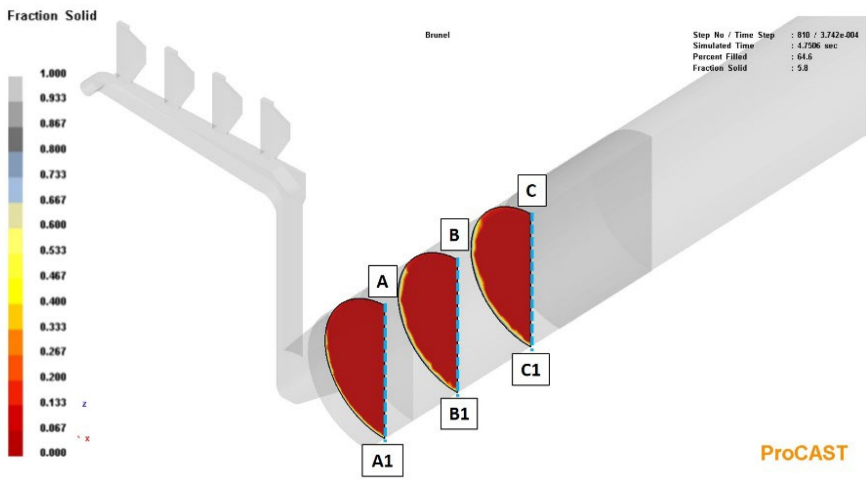

Fig. 15 Solid fraction at piston front in shot sleeve after slow shot phase in CC-HPDC-slice views with Profile-1 in Fig. 12

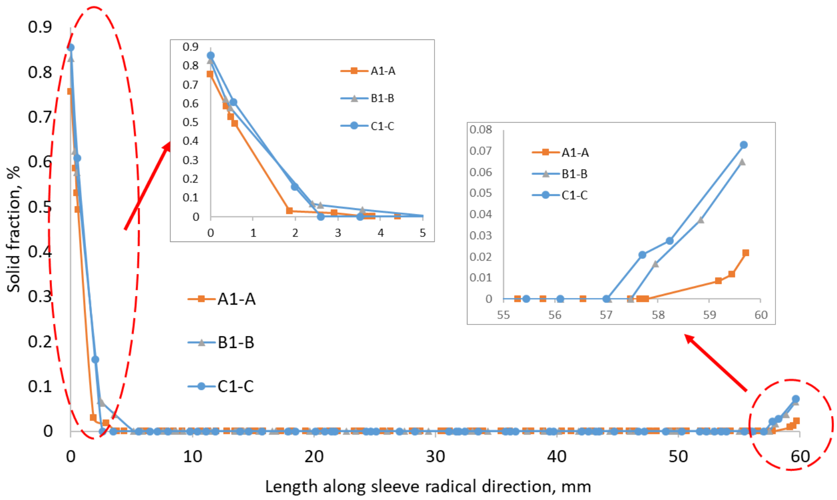

Fig. 16 Solid fraction curves along line A1-A, B1-B and C1-C from Fig. 14

4. Discussion

4.1 Evolution of ESCs amount in shot sleeve with different first stage velocities.

During slow shot phase, the total residence time of the melt inside shot sleeve various with different first stage piston velocities. **Figure 17 (a)-(c)** reveals the solid fraction evolution inside shot sleeve with different piston profiles indicated in **Figure 13**. The value for solid fraction for the mixture in the shot sleeve can be calculated and obtained automatically in the software. According to shot sleeve length, total melt pouring time and piston velocity, the transition point from slow shot to fast shot can be determined, and the final solid fraction before fast shot can be identified in fs curves, as illustrated in **Figure 17**. The critical solid fraction at shot transition point is labelled accordingly.

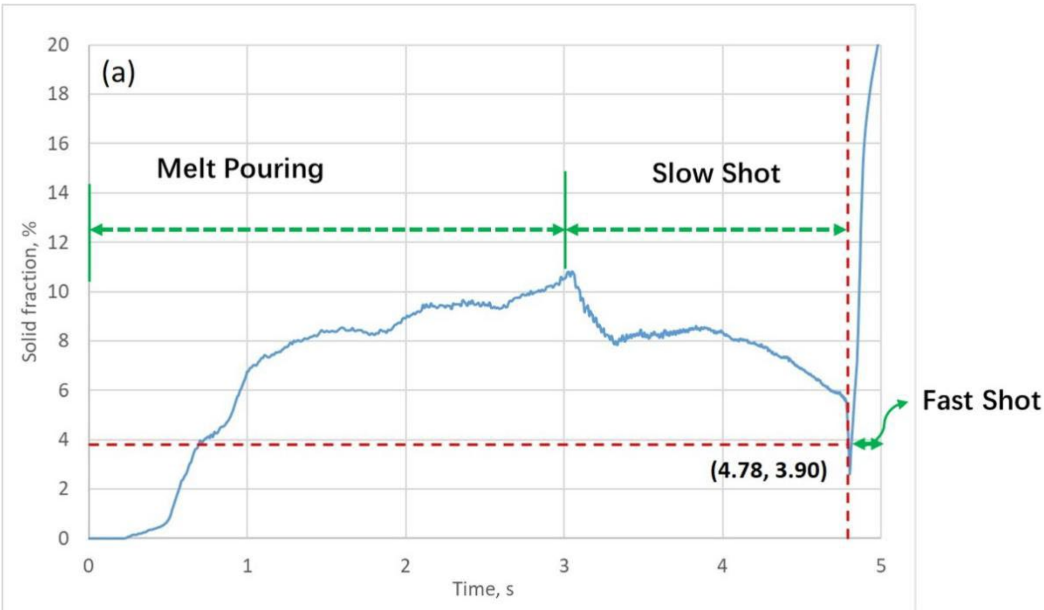

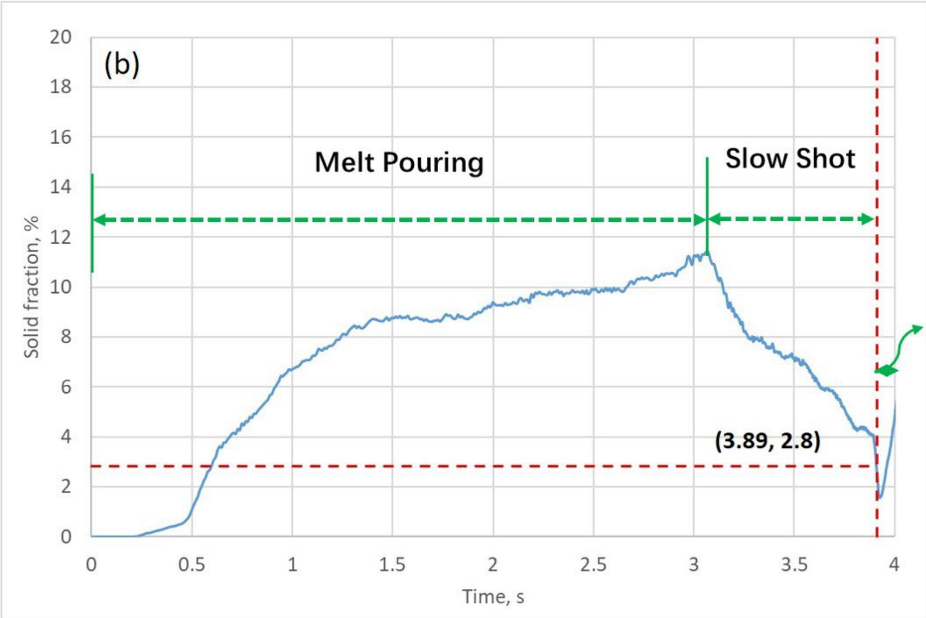

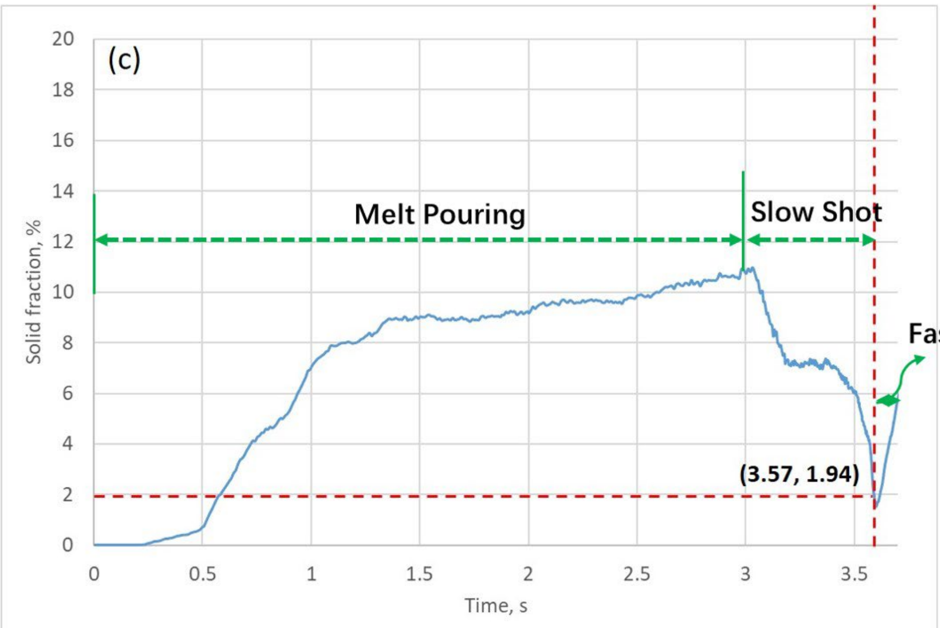

Fig. 17 Evolution of ESCs inside shot sleeve during melt pouring and slow shot stage under various piston profiles indicated in Fig. 13. Solid fraction at transition point from slow shot to fast shot are marked

Before piston movement, the maximum solid fraction inside shot sleeve is shown to reach about 11% after the melt is poured and is continuously cooled by the sleeve wall. As the slow shot stage proceeds, the solid fraction decreases to some extent for a dynamic equilibrium due to the mixing of ESCs with the remaining melt, and it is more obvious with lower piston slow shot velocity. The amount of ESCs remaining in the melt before die filling decreases with increasing slow shot velocity. Considering the initial pouring amount of the alloy, which is 750g, the amount of ESCs remaining in the melt prior to die filling under the three different piston velocity profiles are 29.25g, 21g and 14.55g, respectively. Moreover, it should be noticed that in this model, only the ESCs floating on the melt free surface are assumed to be transported into die cavity, while a portion of those formed on the sleeve wall undergoes remelting to some extent, and the remaining stays in the biscuit, this phenomenon has also been reported in other work [27].

4.2 Evolution of ESCs amount at melt free surface during HPDC process

During the melt injection process, the melt is accumulated at piston front during slow shot phase and is injected into die cavity during the fast shot phase. Meanwhile, a portion of ESCs would float at melt free surface (the fluid flow front in shot sleeve and die cavity, which is illustrated in Figure 8) and end up in die cavity. Subsequently, these ESCs would migrate and distribute in casting and affect the microstructure and mechanical properties of the products [20-22]. Hence, it would be valuable to know the amount of ESCs end up in the die cavity. In this work, the solid fraction curve at the melt free surface is obtained during shot sleeve filling and injection, the time when melt enters die cavity is determined by the transition point from slow shot to fast shot. Accordingly, the fraction of solid being transported into die cavity with free surface can be quantified. The solid fraction curves at the melt free surface with three different piston velocity profiles are shown in **Figure 18 (a)-(c)**. The critical amount of ESCs at slow-fast shot transition point are labelled in figures.

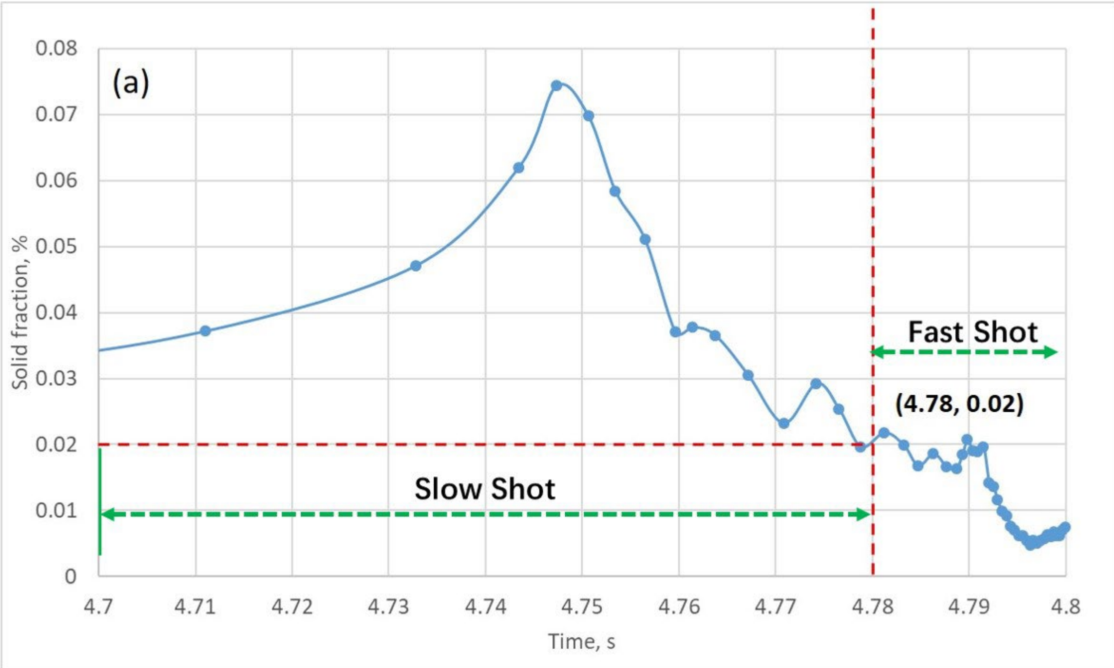

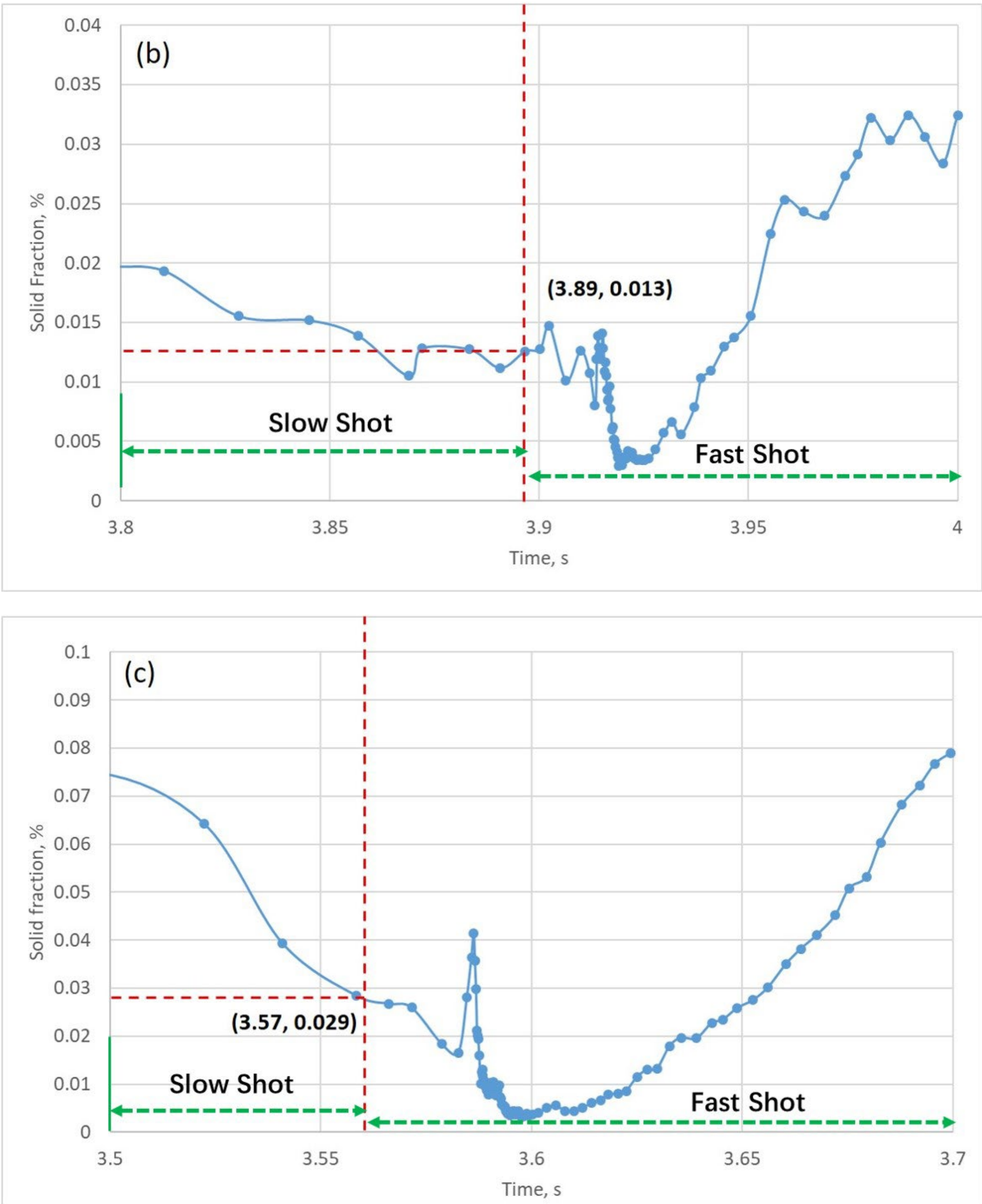

Fig. 18 Evolution of ESCs amount at melt free surface near slow shot-fast shot transition point under various piston profiles indicated in Fig. 12. Solid fraction at transition point from slow shot to fast shot are marked

As is shown in **Figure 18**, solid fraction evolution curve at melt free surface is plotted (only the time interval near slow-fast shot transition point is shown here), which indicates complex flow behavior during HPDC processing. Melt flow and collision or folding of the free surface induced by piston motion would all contribute to variation in the amount of ESCs transported into the die cavity. For this work, the amount of ESCs transported into the die cavity were calculated to be 0.15g, 0.10g and 0.22g, for the three piston velocity profiles respectively. The ESCs transported into the die cavity undergo further solidification, thus affecting the average grain size of the residual microstructure, as previously proven by numerous researchers [23-26].

To further validate the prediction for transported ESCs amount in the die cavity, the microstructures at the cross sections of totally 418 tensile samples (142 for profile-1, 136 for profile-2, 140 for profile-3) were observed using standard optical microscope (OM) method after polishing and etching. A typical microstructure feature of the cross section in a tensile sample is shown in **Figure 19**. It could be seen that the microstructure shows a typical morphology of fine-grain outer layer and relatively coarse-grain central region and a porosity-containing defect band in between. The microstructure mainly comprises of α-Al grains (white), eutectics (grey) and porosities (black). The large, elongated grains with branches are typically ESCs formed in shot sleeve, while the small, spherical grains are formed in the die cavity where there's high cooling rate to promote heterogeneous nucleation. It could be seen that the fraction of large grains increased from skin to central region in the cross section. On this basis, the distribution of grain size was measured using image processing software, the total number of grains analyzed is 452 for profile-1, 518 for profile-2 and 477 for profile-3. The statistical result is summarized in **Figure 20**. To determine the ESCs size range in the die cavity, the microstructures of the solidified alloy in the sleeve is characterized using scanning electron microscopy (SEM), as is indicated in **Figure 21**. It could be seen that the average grain size in the sleeve is above 30 micros, as the ESCs originated from the shot sleeve and would continue their growth after injected into the die cavity. The in-cavity grains whose size were larger than 40 micros and were defined as ESCs. Based on this, the ECSs fractions could be determined from **Figure 20**. The ESCs fraction with piston profile-1 to profile-3 was 1.3%, 1.8% and 2.2%, respectively. In this way, the weight of ESCs that were transported into the die cavity could be deduced and the measured and predicted values were summarized as in **Figure 22**. It could be observed that the prediction about the ESCs fraction in the die cavity agrees to some extent with the measurements, in the future works, it is expected to further develop this model, which will couple the influence of fluid dynamics on the ESCs migration to improve the prediction accuracy.

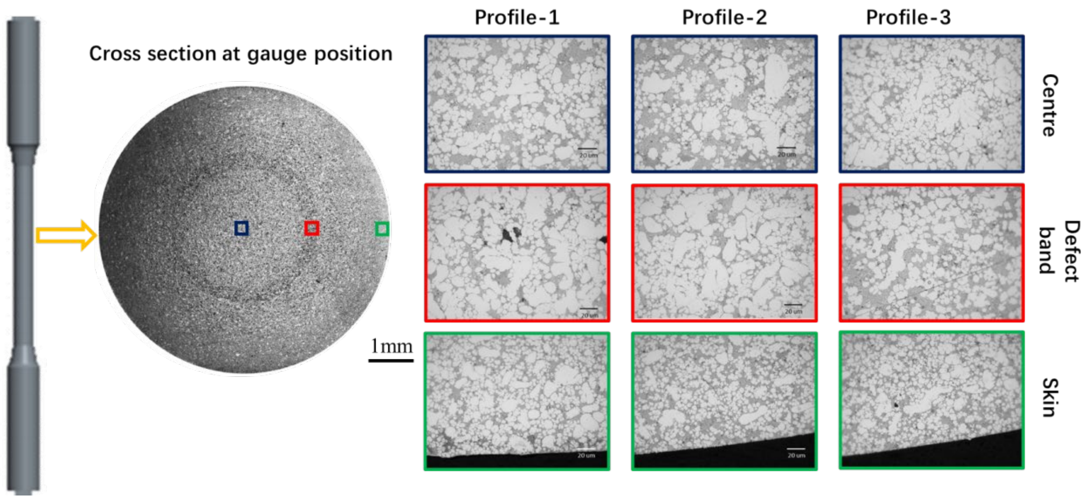

Fig. 19 Microstructures at gauge cross section (left) of tensile bars and enlarged zones (right) from centre, defect band and skin region with different piston profiles

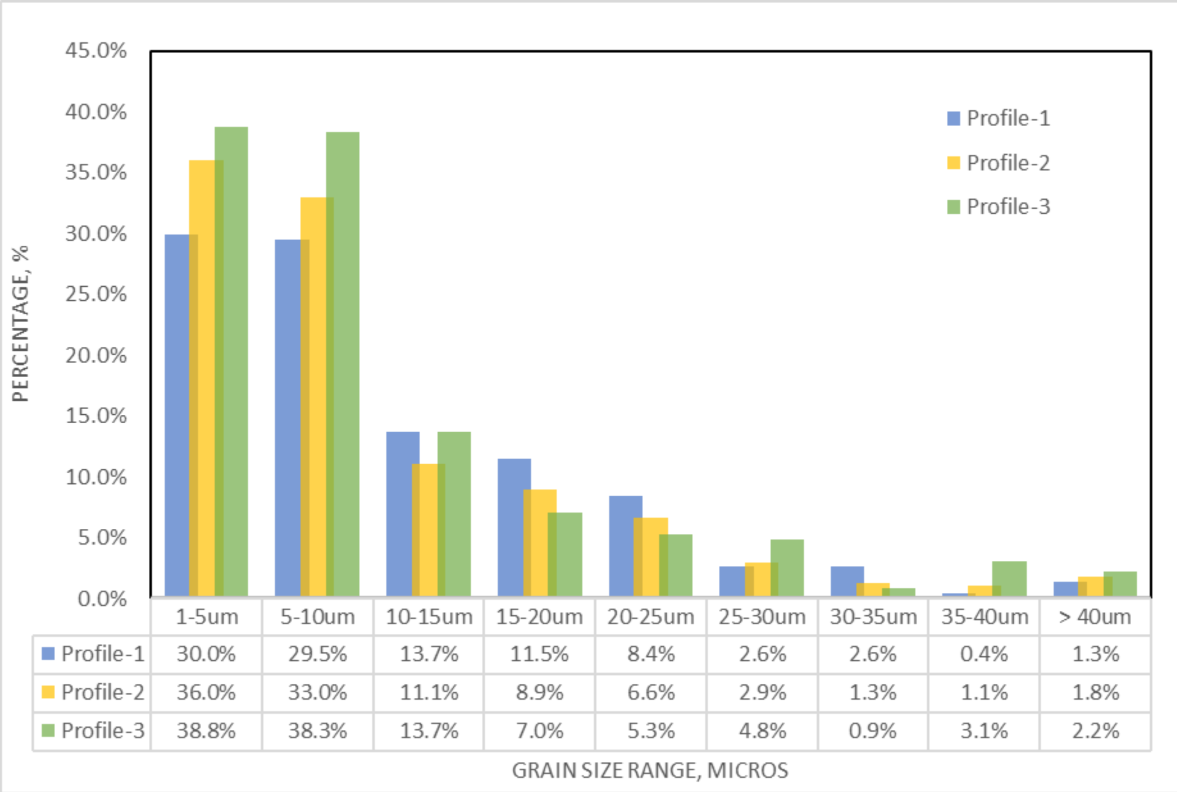

	1-5um	5-10um	10-15um	15-20um	20-25um	25-30um	30-35um	35-40um	> 40um
Profile-1	30.0%	29.5%	13.7%	11.5%	8.4%	2.6%	2.6%	0.4%	1.3%
Profile-2	36.0%	33.0%	11.1%	8.9%	6.6%	2.9%	1.3%	1.1%	1.8%
Profile-3	38.8%	38.3%	13.7%	7.0%	5.3%	4.8%	0.9%	3.1%	2.2%

Fig. 20 Grain size distribution for α-Al in tensile samples with different piston profiles

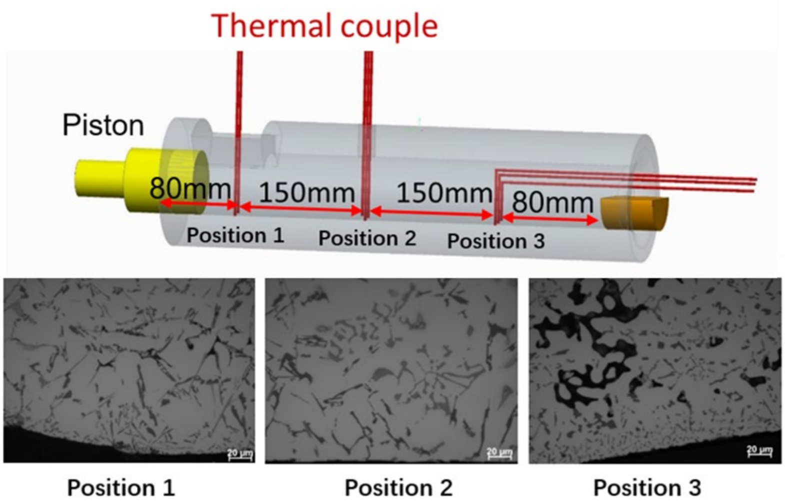

Fig. 21 Characterization of grain formation in the shot sleeve produced with sleeve fill test as shown in Fig. 5

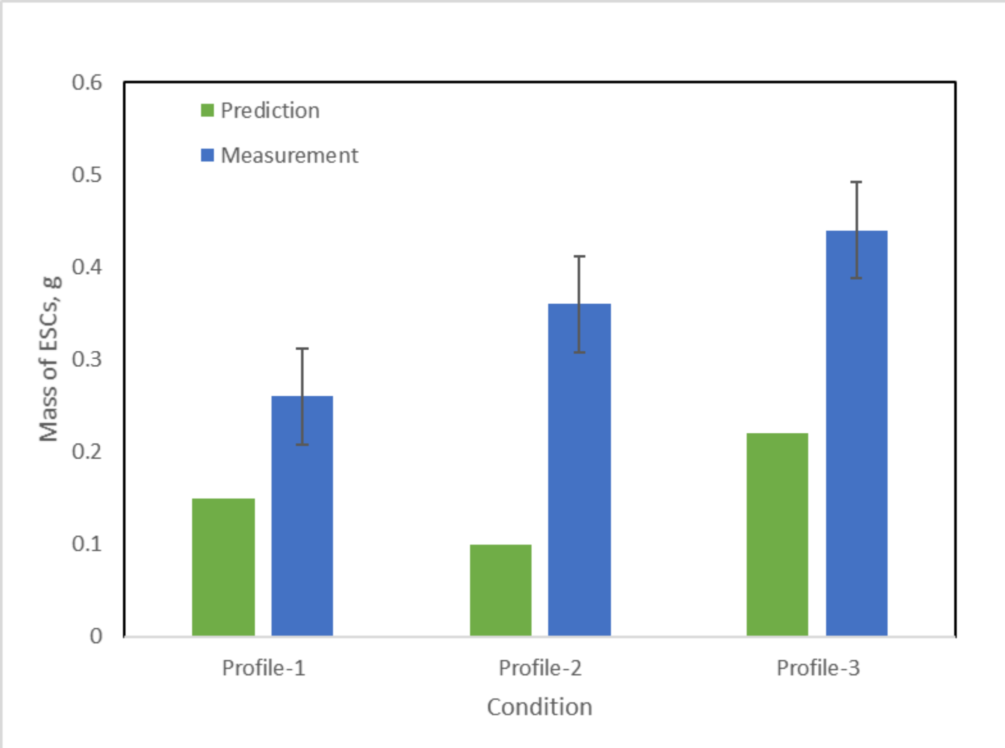

Fig. 22 Comparison between ESCs fractions obtained from measurement and prediction in the die cavity with different piston profiles

5. Conclusions

In this work, the initial solidification behavior of Al-Si alloy THE in shot sleeve of CC-HPDC process is studied combining modelling and experimental methods. Main conclusions are as follows.

1. The filling, heat transfer and solidification process of THE aluminium melt during the CC-HPDC process was simulated in ProCAST, modification of wall functions and interfacial heat transfer coefficients between melt and shot sleeve wall was undertaken considering actual casting condition. Validation against experiments demonstrates good reliability of the model.

2. During shot sleeve filling and before piston movement, a thin layer of solid forms along the length of the shot sleeve with a non-uniform distribution. More ESCs tend to aggregate towards the piston region due to the intensive cooling of the piston, while away from the melt impingement region, solid shell thickness increases due to a transition from turbulent to laminar flow. At the far end of shot sleeve, solid thickness increases due to the cooling of the die.

3. During injection, the solid fraction in the sleeve first increases during the slow shot phase, then, with piston acceleration, some ESCs re-melt. Meanwhile, a portion of remaining ESCs flow into the die cavity along with the melt. The evolution of ESCs in the shot sleeve and those end up in the die cavity with the melt free surface under three sets of piston movement profiles were analyzed quantitatively and validated with materials characterization and statistical measurements.

Acknowledgement

This project is financially supported by EPSRC UK in the EPSRC Centre for Innovative Manufacturing in Liquid Metal Engineering (The EPSRC Centre-LiME).

Conflict of Interest

The authors declare that they have no conflict of interest.

Data Availability

The data used to support the findings of this study are available from the corresponding author upon request.

Reference

1. Y. Lu, F. Taheri and M. Gharghouri: *J. Alloy Compd.*, 2008, vol. 466(1-2), pp. 214-227.

2. Z. Yuan, Z. Guo and S.M. Xiong: *Mater. Charact.*, 2018, vol. 135, pp.278-286.

3. Y. Zhang, J.B. Patel, J. Lazaro-Nebreda and Z. Fan: *JOM*, 2018, vol. 70, pp.2726-2730.

4. H.I. Laukli, C.M. Gourlay and A.K. Dahle: *Metall. Mater. Trans. A*, 2005, vol. 36, pp.805-818.

5. S. Otarawanna, C.M. Gourlay and H.I. Laukli, et al.: *Metall. Mater. Trans. A*, 2009, vol. 40 (7), pp. 1645-1659.

6. H.I. Laukli, O. Lohne and S. Sannes, et al.: *Int. J. Cast Met. Res.*, 2003, vol. 16 (6), pp. 515-21.

7. G. Timelli and A. Fabrizi: *Metall. Mater. Trans. A*, 2014, vol. 45, pp.5486-5498.

8. Z. Fan, M. Xia and H. Zhang, et al.: *Int. J. Cast Metal Res.*, 2009, vol. 22, pp.103-107.

9. Z. Fan, M. Xia and Z. Bian, et al.:, *Mater. Sci. Forum*, 2010, vol. 649, pp. 315-323.

10. S.G. Lee, G.R. Patel and A.M. Gokhale, et al.:, *Scripta Mater*., 2005, vol. 53, pp.851-856.

11. S. Ji, W. Yang and Z. Fan, et al.:, *Mat. Sci. Eng. A-Struct.*, 2013, vol. 566, pp.119-125.

12. K. Dou, E. Lordan, and Y. Zhang et al. *J. Mater. Process. Technol.*, 2021, vol. 296, doi: 10.1016/j.jmatprotec.2021.117193.

13. K. Dou, E. Lordan, Y. J. Zhang et al. *IOP Conf. Ser. Mater. Sci. Eng.*, 2019, vol. 529, p. 012058, doi: 10.1088/1757-899X/529/1/012058.

14. K. Dou, E. Lordan, Y. J. Zhang et al. *J. Manuf. Process.*, 2020, vol. 60, pp. 435–446, doi: 10.1016/j.jmapro.2020.10.062.

15. R. Helenius, O. Lohne, L. Arnberg and H.I. Laukli: *Mat. Sci. Eng. A-Struct.*, 2005, vol. 413, pp.52-55.

16. W. Yu, Y. Cao and S. Xiong: *J. Mater. Sci. Technol.*, 2017, vol. 33(1), pp.52-58.

17. Y. Cao, S. Xiong and Z. Guo: *Acta Metall. Sin.*, 2015, vol. 51, pp.745-752.

18. W. Yu, S. Liang and S. Xiong, et al.: *China Foundry*, 2017, vol. 14, pp.258-264.

19. R. Helenius, O. Lohne, L. Arnberg and H.I. Laukli: *Mat. Sci. Eng. A-Struct.*, 2005, vol., 413, pp.52-55.

20. X.B. Li, S.M. Xiong and Z.P. Guo: *Mat. Sci. Eng. A-Struct.*, 2015, vol. 633, pp.35-41.

21. S. Ferraro and G. Timelli: *Metall. Mater. Trans. B*, 2015, vol. 46, pp.1022-1034.

22. D.R. Gunasegaram, M. Givord, R.G. O'Donnell and B.R. Finnin: *Mat. Sci. Eng. A-Struct.*, 2013, vol. 559, pp.276-286.

23. H.I. Laukli, L. Arnberg and O. Lohne: *Int. J. Cast Metal Res.*, 2005, vol. 18, pp.65-72.

24. B.S. Wang and S. M. Xiong: *T. Nonferr. Metal. Soc*, 2011, vol. 21, pp.767-772.

25. C.M. Gourlay, A.K. Dahle and H.I. Laukli: *Metall. Mater. Trans. A*, 2004, vol. 35, pp.2881-2891.

26. C. Bi, S. Xiong, X. Li and Z. Guo: *Metall. Mater. Trans. B*, 2016, vol. 47, pp.939-947.

27. B.S Wang and S. M. Xiong: *Trans. Nonferrous Met. Soc. China.*, 2011, vol. 21, pp.767-772.